

Phase-driven collapse of the Cooper condensate in a nanosized superconductor

Alberto Ronzani,^{*} Sophie D'Ambrosio, Pauli Virtanen, and Francesco Giazotto[†]
NEST, Istituto Nanoscienze-CNR and Scuola Normale Superiore, I-56127 Pisa, Italy

Carles Altimiras
SPEC, CEA, CNRS, Université Paris-Saclay, CEA-Saclay, 91191 Gif-sur-Yvette, France

Superconductivity can be understood in terms of a phase transition from an uncorrelated electron gas to a condensate of Cooper pairs in which the relative phases of the constituent electrons are coherent over macroscopic length scales [1]. The degree of correlation is quantified by a complex-valued order parameter, whose amplitude is proportional to the strength of the pairing potential in the condensate. Supercurrent-carrying states are associated with non-zero values of the spatial gradient of the phase. The pairing potential and several physical observables of the Cooper condensate can be manipulated by means of temperature, current bias, dishomogeneities in the chemical composition or application of a magnetic field [2]. Here we show evidence of complete suppression of the energy gap in the local density of quasiparticle states (DOS) of a superconducting nanowire upon establishing a phase difference equal to π over a length scale comparable to the superconducting coherence length. These observations are consistent with a complete collapse of the pairing potential in the center of the wire, in accordance with theoretical modeling based on the quasiclassical theory of superconductivity in diffusive systems. Our spectroscopic data, fully exploring the phase-biased states of the condensate, highlight the profound effect that extreme phase gradients exert on the amplitude of the pairing potential. Moreover, the sharp magnetic response observed near the onset of the superconducting gap collapse regime can be exploited to realize ultra-low noise magnetic flux detectors [3].

The physics of superconducting boundaries is an invaluable tool for the investigation of the fundamental properties of matter and for fostering the development of novel devices. From tunnel-type contacts [4] to clean galvanic interfaces dominated by proximity effect [1], the fabrication and manipulation of superconducting boundaries is the enabling feature for the realization of ultra-sensitive magnetometers [5] and electrometers [6], sub-Kelvin electron thermometers and coolers [7], coherent mesoscopic heat current controllers [8, 9], radiation detectors [10], parametric amplifiers [11, 12], qubits [13] and Majorana physics demonstrators [14].

In superconducting electronics, localized geometrical

and compositional inhomogeneities provide preferential pinning points for the establishment of order parameter phase gradients, the distinctive superconducting degree of freedom. This is exemplified by the coherent character of the pair transport between two different Cooper condensates leading to the Josephson effect [15], where the current to phase relation (CPR) is determined by the phase-dependent energy spectrum of weak link-bound states [16]. The latter has been resolved spectroscopically down to the individual mesoscopic channel in atomic contacts [17].

Correspondingly, physical observables in diffusive mesoscopic weak links are dependent on the phase difference between their superconducting boundaries. The phase-driven modulation of the DOS of proximized normal metal weak links is a well known example [18]. Analogous observations have been reported for superconductive wires in the long limit, where partial depairing was induced by spatially uniform phase gradient profiles [19].

On the other hand, phase-biasing a weak link based on a thin superconducting wire in the short limit (i.e., having comparable geometric and coherence length) allows the observation of the reaction of its Cooper condensate to a spatial phase profile well beyond the linear regime. In particular, provided that the state of the Cooper condensate is a single-valued function of the phase difference applied to this weak link, the latter can be polarized with a phase difference equal to π , reaching the non-trivial node of its CPR. In this specific state no supercurrent flows in the Cooper condensate and, by virtue of time-reversal symmetry, its order parameter $\Delta \exp(i\phi)$ is a real-valued and sign-changing function of the spatial coordinate along the wire. Then, as a consequence of continuity, the pairing potential amplitude $\Delta(x)$ must equal zero in some position inside the wire (e.g., the centre in case of symmetric boundaries). A conceptual representation of the mechanism of phase-driven collapse of the order parameter is presented in Figure 1b.

In our experiment, the phase bias on a nanosized aluminum wire is enforced by virtue of magnetic flux quantization in a closed superconducting loop subjected to a magnetic field applied orthogonally [20, 21]. The phase-dependent DOS inside the wire is probed through standard two-wire charge transport spectroscopy via a tunnel-barrier electrode (refer to the schematic in Figure 1a). This type of device is the superconducting-wire analogue of the superconducting quantum interference

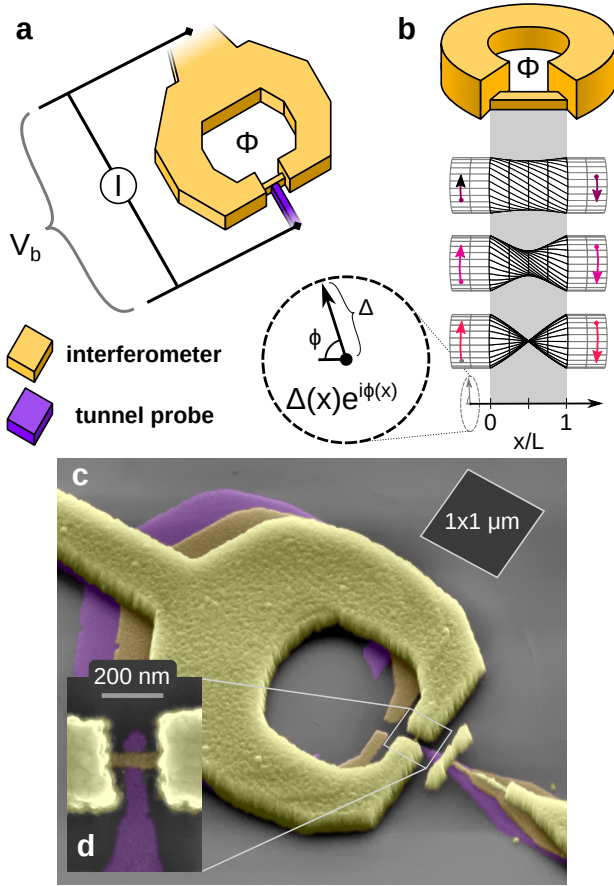


Figure 1. Principle of operation and interferometer design. **a:** Schematic representation of the measurement setup for the transport spectroscopy of a phase-biased superconducting wire. The current-voltage characteristics show the modulation of the local density of states in the latter as a function of the magnetic flux Φ coupled to a compact superconducting loop in clean contact with the wire. **b:** Conceptual picture of the progressive depairing in the middle of the superconducting wire for increasing phase gradient. The position-dependent value of the complex order parameter $\Delta(x) \exp[i\phi(x)]$ is shown as a twisted-wireframe representation of a revolution surface. For a superconducting wire having single-valued current-to-phase relationship, $\Delta(L/2) = 0$ is expected for $\Phi = \Phi_0/2$. **c, d:** Pseudo-colour scanning electron micrographs of, respectively, the interferometer loop and the superconducting wire in a typical device. Here, yellow indicates the 150-nm-thick “interferometer” and 25-nm-thick “nanowire” Al layers; the 15-nm-thick AlOx tunnel probe electrode is shown in purple, realized by oxidizing respectively a Al/Al_{0.98}Mn_{0.02} layer to obtain a superconducting/normal-metal electrode.

proximity transistor (SQUIPT) [22].

In this design, robust phase-biasing performance is ensured by the adoption of a 150-nm-thick aluminum loop of micrometric size, a configuration that proved to be effective in SQUIPTs based on normal-metal weak links of comparable size [3, 23]. Moreover, the pronounced geometric contrast in the cross section of the ring with

respect to the superconducting wire minimizes depairing effects induced by supercurrent concentration at the interfaces between the wire and the thicker superconducting ring [24].

The modulation of the current-vs-voltage $I(V_b)$ characteristics of a typical (wire length $L = 160$ nm) normal-metal tunnel probe device (tunnel resistance $R_T \approx 150$ k Ω) as a function of the applied magnetic flux Φ is presented in Fig. 2. At base temperature ($T = 20$ mK) increasing the magnetic flux bias from $\Phi = 0$ to $\Phi = \Phi_0/2$ results in a 65% suppression of the energy gap in the quasiparticle DOS compared to its zero-field value (panels a,e). Notably, the low-temperature differential conductance characteristics (see Fig. 2e) recorded for $\Phi/\Phi_0 \lesssim 0.25$ are compatible with data reported for specimens in the constant phase gradient regime [19]. This could be expected since in this flux range, the CPR is essentially linear. However, for $\Phi/\Phi_0 \approx 0.5$, a peculiar concentration of quasiparticle states at the edges of the residual energy gap can be inferred from the experimental data. The latter feature, absent in short phase-biased normal-metal wires [23], appears reproducibly between different samples, provided a sufficient phase difference is applied to the short superconducting wire. By increasing the temperature ($T = 300, 500, 700$ mK, panels b-d) the $I(V_b)$ curves show evidence of the progressive suppression of the residual energy gap at $\Phi = \Phi_0/2$. The magnetic modulation of the differential conductance recorded at $T = 650$ mK (panel f) shows the transition between a superconductor/insulator/normal-metal-like response at zero field to an almost ohmic response at $\Phi = \Phi_0/2$.

These observations can be understood by considering the temperature response [25] of the CPR of a weak link based on a superconducting wire in contact with rigid superconducting electrodes. The physical observables of the latter have been calculated in the quasi-classical framework by solving the Usadel equations self-consistently with the pairing amplitude profile. Figure 3 shows a synopsis of modeled physical quantities obtained from a parameter set chosen in accordance with experimental data (refer to the Methods section for details).

As the temperature increases, the current-to-phase relation of the weak link progressively shifts from a multi-valued $I_s(\Phi)$ at low-temperature [characterized by metastable $\Phi = \Phi_0(n + 1/2)$ nodes] to a single-valued CPR functional form reached at $T = 700$ mK. In the latter regime the amplitude of the pairing potential in the centre of the wire can be completely suppressed by applying a phase difference equal to π (panel c).

Simultaneously, the differential conductance as a function of voltage bias, applied magnetic flux and temperature can be computed from the corresponding DOS. In Figure 3d–g, the calculated differential conductance maps are juxtaposed for comparison with data measured at different temperatures. The striking correspondence obtained corroborates the physical interpretation of com-

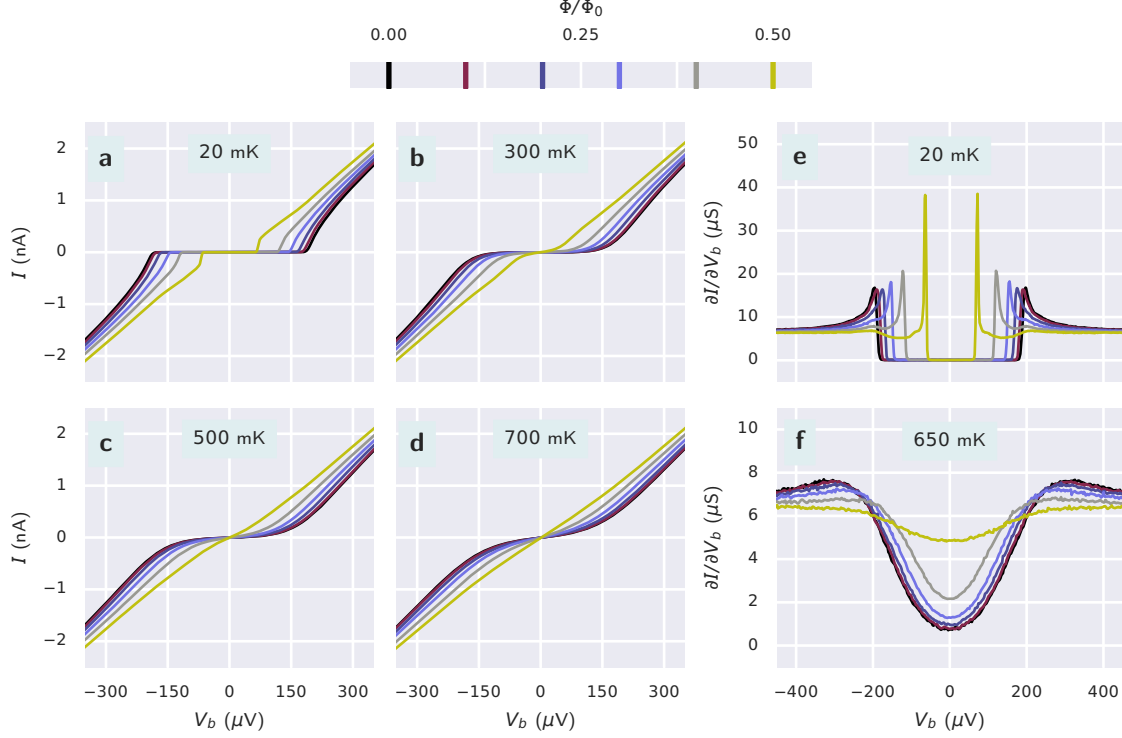


Figure 2. Magneto-electric response of a typical normal-metal tunnel probe device. Different traces are color-coded to six applied magnetic flux values equally spaced in the range $\Phi = 0 \rightarrow \Phi_0/2$. **a–d**: Current-vs-voltage characteristic curves, recorded at lattice temperature $T = 20, 300, 500, 700$ mK, respectively. **e, f**: Differential conductance as a function of voltage bias, recorded at lattice temperature $T = 20, 650$ mK, respectively.

plete pair potential suppression in the superconducting wire for $\Phi/\Phi_0 = 0.5$.

This above interpretation is further confirmed by observations focused on the transition from the unstable to stable π phase bias regime in devices equipped with a superconducting tunnel electrode. The latter, realized by a 15-nm-thick oxidized aluminum film, features a BCS-like DOS characterized by a sizeable superconducting gap $\Delta_{pr} \approx 250 \mu\text{eV}$, typical of thin Al films. As a consequence, the spectroscopic sampling of the DOS in the phase-biased wire does not suffer from the loss of energy resolution due to thermal broadening typical of normal-metal probes. In particular, this setup allows for a direct estimate of the energy gap $\varepsilon_g(\Phi)$ in the probed DOS. At finite temperature, the latter quantity can be derived from the difference between voltage bias values relative to the direct and thermally-activated conductance peaks (found, respectively, at $eV_b = \Delta_{pr} \pm \varepsilon_g$) [26].

Panels a,b in Figure 4 show normalized differential conductance maps recorded for a representative device characterized by a $L = 210$ nm superconducting wire in contact with a $R_T = 15$ k Ω superconducting tunnel elec-

trode. The mapping is focused on voltage bias values corresponding to the superconducting gap in the probe ($eV_b \approx \Delta_{pr}$) and with coupled magnetic flux applied in a minute range centered around $\Phi_0/2$. By inspecting the flux modulation of the direct ($eV_b < \Delta_{pr}$) and thermally-activated ($eV_b > \Delta_{pr}$) conductance peaks, an incomplete suppression of $2\varepsilon_g \simeq 40 \mu\text{eV}$ can be inferred from data recorded at $T = 0.9$ K (panel a). Within a 100 mK temperature increase, we observe the merging of the direct and thermally-activated peaks at $\Phi/\Phi_0 = 0.5$ and $eV_b = \Delta_{pr}$, the direct evidence of the full suppression of the energy gap in the probed quasiparticle DOS. We interpret this as the confirmation that the increase in temperature has driven the CPR of the weak link to the single-valued regime, leading to a complete collapse of the amplitude of the pairing potential in the center of the wire for $\Phi/\Phi_0 = 0.5$. In this case, the temperature value for this transition is higher than for the normal-probe interferometer (Figures 2 and 3) as expected from the difference in the respective lengths of the wires, in agreement with the theory.

The steep character of the magnetic flux dependence

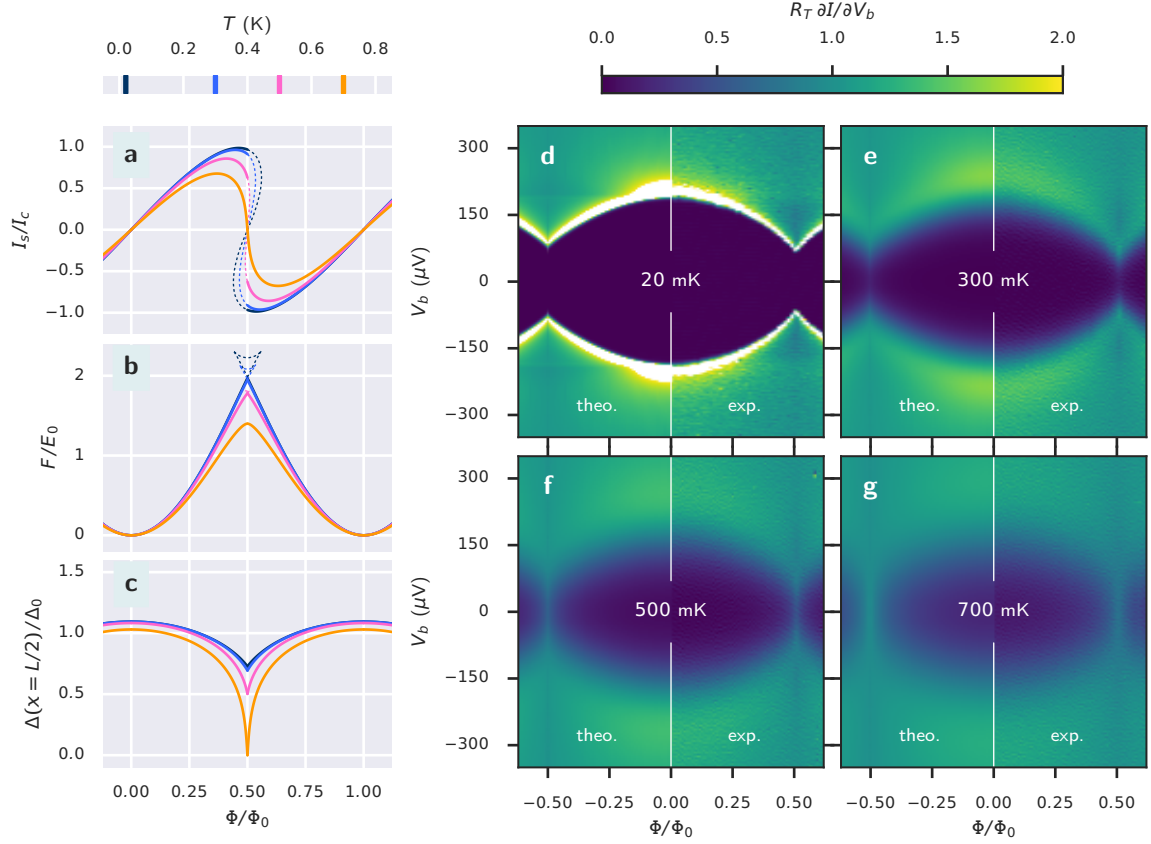


Figure 3. Results for the modelization of the superconducting nanowire according to parameters inferred from experimental data. **a**: Circulating supercurrent I_s normalized to the zero-temperature value of the critical current of the wire (I_c). **b**: Interferometer free energy F normalized to $E_0 = I_c \Phi_0 / 2\pi$. **c**: Pairing potential amplitude $\Delta(x = L/2)$ in the center of the superconducting nanowire normalized to the zero-temperature value of the pairing potential amplitude in the interferometer loop (Δ_0). In panels **a**–**c**, different traces are color-coded to the temperature values $T = 20, 300, 500, 700$ mK and show the modulation of the respective quantity as a function of the magnetic flux Φ applied to the interferometer. Dotted branches in panels **a**, **b** represent theoretical solutions corresponding to thermodynamically unstable interferometer states. **d**–**g**: Normalized differential conductance of the normal-metal tunnel probe device as a function of the applied magnetic flux and voltage bias V_b at lattice temperature $T = 20, 300, 500, 700$ mK, respectively. The halves of each colormap plot allow the comparison between theoretical predictions (left) and experimental data (right).

of the pairing potential suppression suggests to exploit these devices for highly-sensitive magnetometry applications. Inspection of voltage traces recorded at $T = 1$ K under constant current bias I_b from the representative superconducting-probe device (Figure 4, panel c) reveals abrupt but continuous voltage response in a minute magnetic flux range close to $\Phi/\Phi_0 = 0.5$. Here, the different traces indicate $I_b \in [4.3, 4.4]$ nA, a range corresponding to the quasiparticle current measured in the voltage-biased setup, with $V_b \approx \Delta_{pr}/e = 250 \mu V$. The corresponding flux-to-voltage responsivity characteristics (panel d) obtain values as large as $\sim 27 \text{ mV}/\Phi_0$, which are unparalleled in this class of devices [3, 23]. In a simple DC-biased setup, magnetic flux resolution figures as low as $250 \text{ n}\Phi_0/\sqrt{\text{Hz}}$, limited by shot noise intrinsic to the tunnel-probe readout, have been measured in the $0.1 - 100$ Hz range (see Supplementary material).

In summary, we have presented a robust and reproducible means of suppressing the order parameter amplitude of the Cooper condensate inside a nanosized superconductor. Our observations are consistent with established theory. Reaching the complete flux modulation of the energy gap in the DOS inside the superconducting wire marks the transition between the *intrinsic*-like and *Josephson*-like regime. The corresponding temperature-dependent modulation of the CPR from a multi-valued locus to a proper single-valued form entails, at the crossover, a strong dependence of the physical observables on the applied magnetic flux for $\Phi \approx \Phi_0/2$. Yet, this property has been applied for the realization of ultra-sensitive small-area quantum magnetometers. More generally, this work provides experimental coverage of the fundamental consequences of the self-consistency requirement on the order parameter in spatially inhomoge-

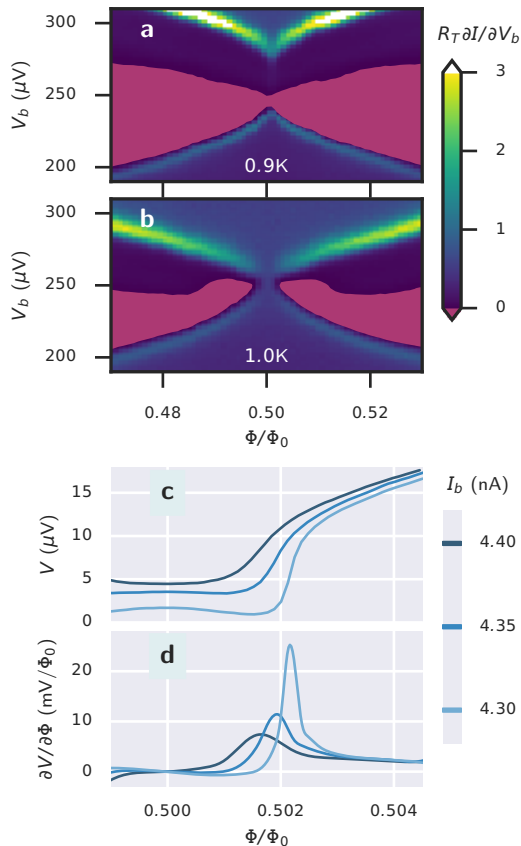


Figure 4. Magneto-electric response of a typical superconducting tunnel probe device. **a, b**: Normalized differential conductance as a function of the applied magnetic flux and voltage bias, recorded at lattice temperature $T = 0.9, 1.0 K$, respectively. The region showing negative differential conductance is indicated in magenta. **c, d**: Respectively, voltage response (arbitrary offset) and corresponding flux-to-voltage transfer function for $\Phi \approx \Phi_0/2$, recorded at temperature $T = 1.0 K$. The device is here operated under fixed current bias values $I_b = 4.30, 4.35, 4.40$ nA.

neous superconductors. Finally, our design might be suitable as a testbed for the generation and investigation of a spatially-locked “phase-slip center”. Another exciting perspective is to investigate whether the multi-valued regions of the CPR are reachable in pulsed phase experiments.

ACKNOWLEDGEMENTS

We acknowledge funding from the European Research Council under the European Unions Seventh Framework Program (FP7/2007-2013)/ERC Grant agreement No. 615187-COMANCHE, the Italian Ministry of Education, University and Research (MIUR) through the program FIRB-RBFR1379UX and the Tuscany Region through the CNR joint project “PROXMAG”. C.A. ac-

knowledges discussions with H. Pothier, P. Joyez and S. Bergeret at the root of the project.

METHODS

Fabrication protocols and experimental set-up

The devices have been fabricated by directional metallic thin film deposition through a self-aligned suspended mask. The latter is obtained by electron beam lithography on a positive tone resist bilayer (1000 nm copolymer / 100 nm poly-methyl metacrylate) spun on an oxidized Si wafer. After the development of the resist bilayer, the substrate is loaded in a ultra-high vacuum (base pressure $\approx 10^{-9}$ Torr) electron beam evaporator, where an initial 15-nm-thick layer of 5N-Al/ $Al_{0.98}Mn_{0.02}$ is deposited at 40° to realize a superconducting/normal-metal probe electrode, respectively. A subsequent controlled exposition (300 s) to a pure O_2 atmosphere with pressure values in the $10 \div 100$ mTorr range yields tunnel junctions having specific resistance in the $20 \div 200 \Omega \mu m^2$ range. The superconducting interferometer is evaporated on top of the tunnel electrode as a 25-nm-thick Al layer at 20° , followed by a 150-nm-thick Al layer at normal incidence.

After chemical lift-off in acetone followed by rinsing in isopropyl alcohol, the samples are inspected in a scanning-electrode microscope. Suitable devices are wire-bonded on a 24 pin dual-in-line ceramic chip carrier, which is then loaded in a filtered $^3He/^4He$ dilution refrigerator (Oxford Instruments, mod. Triton 200) for the magneto-electric characterization down to 20 mK. In the latter, the magnetic field is applied orthogonal to the substrate by a custom-built superconducting electromagnet driven by a low-noise programmable current source (Keythley model 2600).

Low-noise current / voltage bias sources (a lithium battery in series with a 200 M Ω impedance and a Yokogawa GS200, respectively) are coupled with room-temperature voltage / current preamplifiers (NF Corporation LI-75A and DL Instruments 1201, respectively) to realize the DC readout. For normal-metal tunnel electrode devices the differential conductance is recorded with lock-in amplification (Stanford research model 830) with 4 μV voltage excitation (rms).

Theoretical model

We model the properties of the superconducting wire embedded in the ring by the quasiclassical Green function model [27], assuming a quasi-1D geometry. The spectral angle θ and phase χ are solved from the Usadel equa-

tions [28]

$$\hbar D \partial_x^2 \theta = -2iE \sinh \theta + \frac{D(\partial_x \chi)^2}{2} \sinh 2\theta \quad (1)$$

$$+ 2i|\Delta| \cos(\phi - \chi) \cosh \theta,$$

$$\hbar D \partial_x \cdot (\partial_x \chi \sinh^2 \theta) = -2i|\Delta| \sin(\chi - \phi) \sinh \theta, \quad (2)$$

where D is the diffusion constant. We assume the contacts between the wire and the ring have nonzero resistance, and model them with the Kupriyanov–Lukichev boundary conditions [29]

$$\mp r \sinh \theta \partial_x \chi = \sin(\chi - \chi_\mp) \sinh \theta_\mp, \quad (3)$$

$$\mp r \partial_x \theta = \sinh \theta \cosh \theta_\mp - \cos(\chi - \chi_\mp) \cosh \theta \sinh \theta_\mp, \quad (4)$$

at the left (−) and right (+) contacts. The parameter $r = R_I/r_w$ is the ratio between the interface resistance R_I and the resistance per length r_w of the wire. The values $\theta_\pm = \text{artanh}(|\Delta_r(T)|/E)$, $\chi_- = 0$, $\chi_+ = \varphi$ are the values of the angles inside the superconducting ring. Here, the $\Delta_r(T)$ value of order parameter in the ring is assumed to be BCS-like, determined by the critical temperature $T_{c,r}$. We neglect proximity effect in the ring, and assume it is unperturbed by the weak link.

The normalized DOS $N(E, x) = \text{Re} \cosh \theta(E, x)$ and supercurrent $I_s = A\sigma \int_{-\infty}^{\infty} dE \text{Im}[\partial_x \chi \sinh^2 \theta] \tanh \frac{E}{2k_B T}$ are obtained from the solutions. The order parameter $\Delta = |\Delta|e^{i\phi}$ is obtained from the self-consistency relation,

$$|\Delta| \ln \frac{T}{T_{c,w}} = 2\pi i k_B T \sum_{\omega_n > 0} \left[e^{i(\chi - \phi)} \sinh \theta - \frac{|\Delta|}{E} \right]_{E=i\omega_n}, \quad (5)$$

where $T_{c,w}$ is the critical temperature of the wire, and $\omega_n = \pi k_B T(2n + 1)$ are the discrete Matsubara energies. Self-consistent determination is required for current conservation.

The solution to Eq. (5) becomes multivalued when $L \gtrsim \xi_0$. To trace the solution branch $(\varphi, \Delta(x))$, in this case, we apply the pseudo-arclength continuation method [30]. The method generates the next point $(\varphi_{k+1}, \Delta_{k+1}(x))$ based on previous solutions, by requiring that $\Delta_{k+1}(x)$ satisfies Eq. (5), and that the phase difference φ_{k+1} , which is also considered unknown, satisfies a pseudo-arclength condition. This condition is an approximate form for requiring the distance from the previous solution, $s = \eta|\varphi_{k+1} - \varphi_k|^2 + (2 - \eta)|\Delta_{k+1} - \Delta_k|_2^2$ be constant $s \approx s_0$, where $0 < \eta < 2$ is the weight factor and s_0 the step size.

In the comparison with experimental data, the relation between applied magnetic flux Φ and phase difference φ is assumed non-linear, with $\Phi/\Phi_0 = \varphi/2\pi + \beta_L I_s(\varphi)/I_c$, where I_c is the low-temperature value of the critical current and $\beta_L = \mathcal{L}I_c/\Phi_0$ accounts for nonzero ring inductance \mathcal{L} . The thermodynamically stable solution is determined as the one that minimizes the

free energy $F(\varphi) = \frac{\Phi_0}{2\pi} \int_0^\varphi d\varphi' I_s(\varphi') + \mathcal{L}I_s^2(\varphi)/2$. The normalized differential conductance $R_T \partial I/\partial V_b$ is calculated from the probe quasiparticle current $I(V_b, \Phi, T) = 1/(eR_T) \int dE \dot{N}(E, \Phi, T)[f_0(E - eV_b) - f_0(E)]$, where $f_0(E) = [1 + \exp(E/k_B T)]^{-1}$ is the Fermi-Dirac distribution function at temperature T and $\dot{N}(E, \Phi, T) = 2/L \int_{L/4}^{3L/4} N(E, x)_{T,\Phi} dx$ is the wire DOS averaged over the typical physical length sampled by the probe.

The datasets in Figure 3 have been generated assuming the values $T_{c,w} = 1.4\text{K}$ and $T_{c,r} = 1.25\text{K}$ for the critical temperature of the wire and the ring, respectively. The modeled diffusive weak link has normalized length $L/\xi_0 = 1.7$, corresponding to $\xi_0 = \sqrt{\hbar D/\Delta_0} = 95\text{nm}$ for a physical length $L = 160\text{nm}$. The interfaces of the wire are modeled with a non-ideality coefficient $r = 0.75$. Optimal agreement with the observed flux modulation shape is obtained by letting $\beta_L = 0.03$, consistent with $I_c \approx 18\mu\text{A}$, assuming $\mathcal{L} = 3.5\text{pH}$ (numerical estimate of the inductance of the superconducting loop including both geometric and kinetic contributions, with magnetic penetration depth $\lambda_\perp \approx 60\text{nm}$. FastHenry version 3.0wr by S. R. Whiteley, available from <http://wrcad.com>).

* alberto.ronzani@sns.it

† francesco.giazotto@sns.it

- [1] P.-G. De Gennes, *Superconductivity of metals and alloys*, Advanced book classics (Advanced Book Program, Perseus Books, Reading, Mass, 1999).
- [2] M. Tinkham, *Introduction to Superconductivity* (Courier Corporation, 1996).
- [3] A. Ronzani, C. Altimiras, and F. Giazotto, “Highly Sensitive Superconducting Quantum-Interference Proximity Transistor,” *Physical Review Applied* **2**, 024005 (2014).
- [4] I. Giaever, “Electron Tunneling Between Two Superconductors,” *Physical Review Letters* **5**, 464–466 (1960).
- [5] D. Vasyukov, Y. Anahory, L. Embon, D. Halbertal, J. Cuppens, L. Neeman, A. Finkler, Y. Segev, Y. Myasoedov, M. L. Rappaport, M. E. Huber, and E. Zeldov, “A scanning superconducting quantum interference device with single electron spin sensitivity,” *Nature Nanotechnology* **8**, 639–644 (2013).
- [6] R. J. Schoelkopf, P. Wahlgren, A. A. Kozhevnikov, P. Delsing, and D. E. Prober, “The Radio-Frequency Single-Electron Transistor (RF-SET): A Fast and Ultra-sensitive Electrometer,” *Science* **280**, 1238–1242 (1998).
- [7] T. T. Giazotto, F. Heikkilä, A. Luukanen, A. M. Savin, and J. P. Pekola, “Opportunities for mesoscopies in thermometry and refrigeration: Physics and applications,” *Reviews of Modern Physics* **78**, 217–274 (2006).
- [8] F. Giazotto and M. J. Martínez-Pérez, “The Josephson heat interferometer,” *Nature* **492**, 401–405 (2012).
- [9] M. J. Martínez-Pérez, A. Fornieri, and F. Giazotto, “Rectification of electronic heat current by a hybrid thermal diode,” *Nature Nanotechnology* **10**, 303–307 (2015).
- [10] P. K. Day, H. G. LeDuc, B. A. Mazin, A. Vayonakis, and J. Zmuidzinas, “A broadband superconducting detector suitable for use in large arrays,” *Nature* **425**, 817–821

- (2003).
- [11] B. Ho Eom, P. K. Day, H. G. LeDuc, and J. Zmuidzinas, “A wideband, low-noise superconducting amplifier with high dynamic range,” *Nature Physics* **8**, 623–627 (2012).
 - [12] C. Macklin, K. O’Brien, D. Hover, M. E. Schwartz, V. Bolkhovskiy, X. Zhang, W. D. Oliver, and I. Siddiqi, “A near-quantum-limited Josephson traveling-wave parametric amplifier,” *Science* **350**, 307–310 (2015).
 - [13] J. Clarke and F. K. Wilhelm, “Superconducting quantum bits,” *Nature* **453**, 1031–1042 (2008).
 - [14] V. Mourik, K. Zuo, S. M. Frolov, S. R. Plissard, E. P. A. M. Bakkers, and L. P. Kouwenhoven, “Signatures of Majorana Fermions in Hybrid Superconductor-Semiconductor Nanowire Devices,” *Science* **336**, 1003–1007 (2012).
 - [15] B. D. Josephson, “Possible new effects in superconductive tunnelling,” *Physics Letters* **1**, 251 – 253 (1962).
 - [16] A. A. Golubov, M. Yu. Kupriyanov, and E. Il’ichev, “The current-phase relation in Josephson junctions,” *Reviews of Modern Physics* **76**, 411–469 (2004).
 - [17] L. Bretheau, Ç. Ö. Girit, H. Pothier, D. Esteve, and C. Urbina, “Exciting Andreev pairs in a superconducting atomic contact,” *Nature* **499**, 312–315 (2013).
 - [18] H. Le Sueur, P. Joyez, H. Pothier, C. Urbina, and D. Esteve, “Phase Controlled Superconducting Proximity Effect Probed by Tunneling Spectroscopy,” *Physical Review Letters* **100**, 197002 (2008).
 - [19] A. Anthore, H. Pothier, and D. Esteve, “Density of States in a Superconductor Carrying a Supercurrent,” *Physical Review Letters* **90** (2003).
 - [20] R. Doll and M. Näbauer, “Experimental Proof of Magnetic Flux Quantization in a Superconducting Ring,” *Physical Review Letters* **7**, 51–52 (1961).
 - [21] B. S. Deaver and W. M. Fairbank, “Experimental Evidence for Quantized Flux in Superconducting Cylinders,” *Physical Review Letters* **7**, 43–46 (1961).
 - [22] F. Giazotto, J. T. Peltonen, M. Meschke, and J. P. Pekola, “Superconducting quantum interference proximity transistor,” *Nature Physics* **6**, 254–259 (2010).
 - [23] S. D’Ambrosio, M. Meissner, C. Blanc, A. Ronzani, and F. Giazotto, “Normal metal tunnel junction-based superconducting quantum interference proximity transistor,” *Applied Physics Letters* **107**, 113110 (2015).
 - [24] R. Vijay, E. M. Levenson-Falk, D. H. Slichter, and I. Siddiqi, “Approaching ideal weak link behavior with three dimensional aluminum nanobridges,” *Applied Physics Letters* **96**, 223112 (2010).
 - [25] K. K. Likharev, “Superconducting weak links,” *Reviews of Modern Physics* **51**, 101–159 (1979).
 - [26] M. Meschke, J. T. Peltonen, J. P. Pekola, and F. Giazotto, “Tunnel spectroscopy of a proximity Josephson junction,” *Physical Review B* **84**, 214514 (2011).
 - [27] W. Belzig, F. K. Wilhelm, C. Bruder, G. Schön, and A. D. Zaikin, “Quasiclassical Green’s function approach to mesoscopic superconductivity,” *Superlattices and Microstructures* **25**, 1251–1288 (1999).
 - [28] P. Virtanen, A. Ronzani, and F. Giazotto, “Spectral characteristics of a fully superconducting SQUIPT,” *Physical Review Applied* **6**, 054002 (2016).
 - [29] M. Yu. Kupriyanov and V. F. Lukichev, “Influence of boundary transparency on the critical current of ”dirty” SS’S structures,” *JETP* **67**, 1163 (1988).
 - [30] H. B. Keller, “Numerical solution of bifurcation and non-linear eigenvalue problems,” *Applications of bifurcation theory* **1**, 359–384 (1977).

Phase-driven collapse of the Cooper condensate in a nanosized superconductor — Supplementary Information

arXiv:1611.06263v1 [cond-mat.supr-con] 18 Nov 2016

MAGNETOMETRIC PERFORMANCE

In the main article's body it has been shown that superconducting-wire SQUIPT magnetometers exhibit very pronounced flux-to-voltage responsivity figures when their current-phase relation transitions from multi-valued to single-valued regime. Here we expand on this application by assessing in detail the magnetometric properties of a complete setup based on this type of device, as illustrated in Figure 1. Notably, the analysis of the cross-correlation between the output signals of two parallel amplification chains connected to the same device allows to distinguish amplifier-limited magnetic flux resolution performance from noise sources intrinsic to the readout scheme.

Figure 2 shows a summary of the voltage response of the representative superconducting probe device for $\Phi \approx \Phi_0/2$, measured at temperature $T = 1\text{K}$ under fixed current $I_b = 4.35\text{nA}$. The noise characteristic of the readout/amplifier system can be assessed by tuning the applied magnetic flux to $\Phi = \Phi_0/2$, where the voltage response is null to the first order in Φ . In this configuration (panel **d**) the power spectral density profiles of the individual preamplifiers (green/blue traces) are only barely higher than their nominal datasheet values, whereas the cross-spectral density (black trace) converges to a profile $\mathcal{X}_{12}(f)$ consistent with the following model (gray shade):

$$\mathcal{X}_{12}(f) = \sqrt{v_a^2 + R_d^2 \frac{2eI_b}{|1 + 2\pi i f R_d C|^2}} \quad , \quad (1)$$

where $v_a = 0.7\text{nV}/\sqrt{\text{Hz}}$ is a white noise background, e is the elementary charge, $R_d = \partial V/\partial I_b$ is the differential resistance and $C = 26\text{nF}$ is the effective shunt capacitance consistent with the noise roll-off observed for $f \approx 100\text{Hz}$. This simple model, based on the quadrature summation of RC-filtered tunnel shot noise with an amplifier-dependent white noise background is sufficient to describe \mathcal{X}_{12} data recorded for $0.3 < f < 300\text{Hz}$.

In Figure 2, a comparison between panel **b** and **c** shows that the peak in the flux-to-voltage transfer function is associated with a corresponding peak in the differential resistance of the device ($\Phi/\Phi_0 = 0.502$). On the other hand, the latter is suppressed with $\Phi/\Phi_0 > 0.5025$, while the flux-to-voltage transfer function maintains appreciable levels. Panel **e** shows indeed that at the working point associated with maximal responsivity, the power spectral density of the individual amplifiers is basically indistinguishable from the cross-correlated spectrum, *i.e.*, the v_a term is negligible in Equation 1. Here, the high value of R_d induces both a

Φ	$\partial V/\partial \Phi$	R_d	noise floor		bandwidth
Φ_0	mV/ Φ_0	k Ω	nV/ $\sqrt{\text{Hz}}$	n $\Phi_0/\sqrt{\text{Hz}}$	Hz
0.5	0.0	36.7	1.5	—	167
0.502	11.3	117.	4.4	390	52
0.5025	4.6	26.2	1.2	260	234

Table I. Summary of magnetometric figures for the working points in Figure 2.

reduction in the available bandwidth and an increase of the shot-noise contribution to the observed voltage spectral density. By contrast panel **f**, corresponding to a working point ($\Phi/\Phi_0 = 0.5025$) characterized by a significantly lower value of R_d , demonstrates a $\mathcal{X}_{12}(f)$ profile characterized not only by wider available RC bandwidth, but also slightly better signal to noise ratio (as suggested by the shape of the 1.3 Hz signal peak). This difference in performance can be more quantitatively appreciated by renormalizing the spectral density profiles from voltage to magnetic flux units by means of the flux-to-voltage transfer function values. The results are shown in Figure 3. A summary of the performance figures for the different working points is reported in Table I.

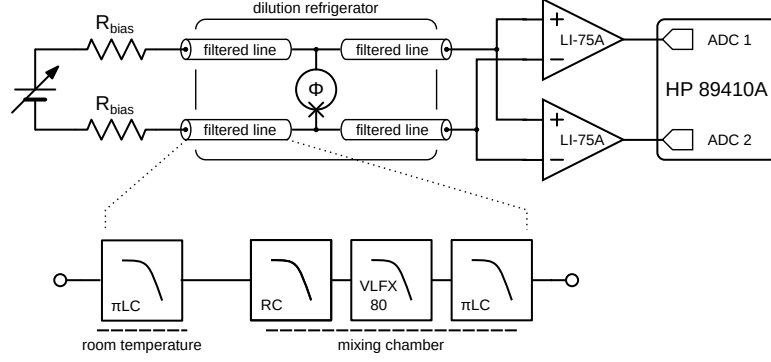


Figure 1. Functional schematic of the setup adopted for the characterization of the noise-equivalent flux level of SQUIPT magnetometers. The voltage response of the latter is probed in a 4-wire configuration where the current bias is provided by an adjustable battery-powered voltage source in series with bias resistors $R_{bias} = 100 \text{ M}\Omega$. The device is housed in a copper enclosure thermally anchored to the mixing chamber of a helium dilution refrigerator. The latter is equipped with identical electrical DC lines filtered as follows: room-temperature $\text{LC}(\pi)$ lowpass filter (Oxley FLT/P/5000), two-pole RC lowpass (room-temperature values: $R = 500 \Omega$, $C = 47 \text{ nF}$) at the mixing chamber followed by high-rejection multistage lowpass (Minicircuits VLFX-80) in series with a $\text{LC}(\pi)$ filter (Oxley SLT/P/5000) at the sample's enclosure. The magnetic flux Φ linked to the interferometer loop is applied by a superconducting magnet surrounding the sample stage and powered by a low-noise programmable current source (Keythley model 2600, not shown). The voltage difference across the device is amplified by two separate battery-powered room-temperature differential voltage amplifiers (NF Corporation model LI-75A), whose outputs are digitized independently as the inputs of a vector signal analyzer (HP model 89410A). The latter computes the power spectral density of each input channel as well as the cross-spectral density between them.

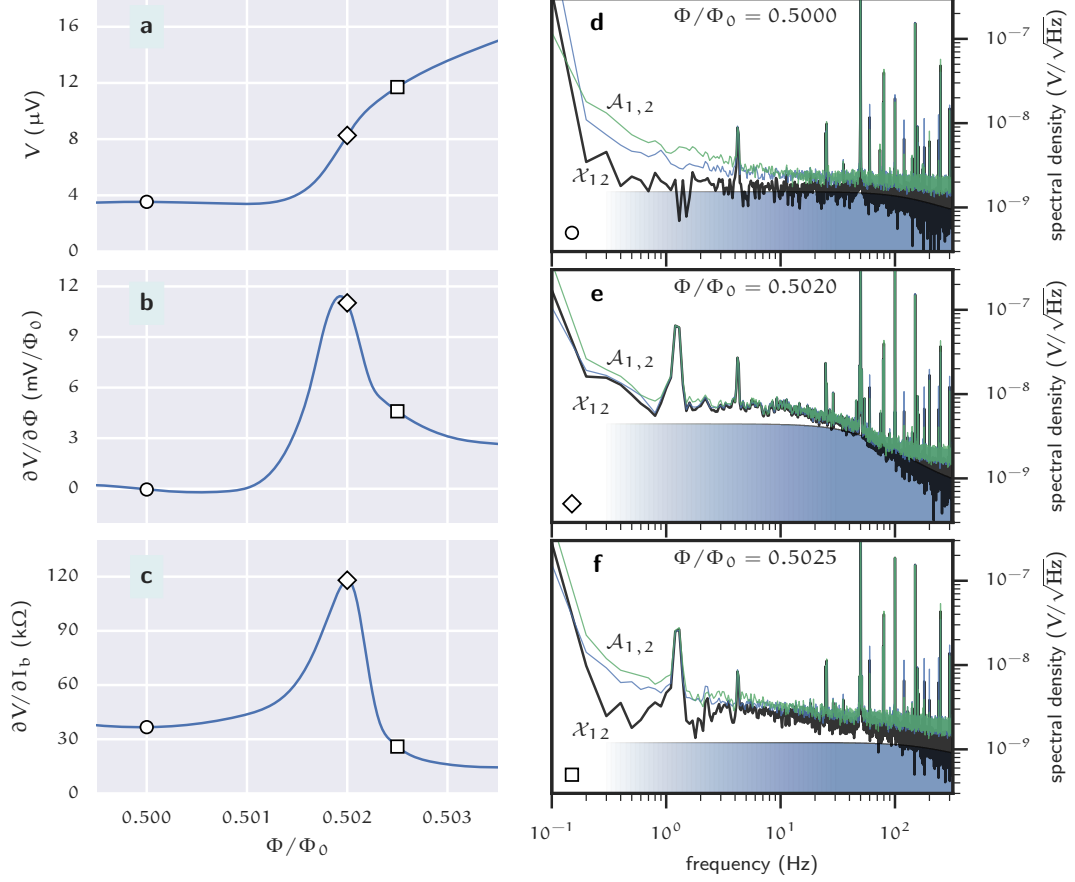


Figure 2. Summary of the magnetoelectric response figure of a typical superconducting-probe device recorded at temperature $T=1\text{K}$ and current bias $I_b = 4.35\text{ nA}$. The datasets shown here expand on the corresponding data presented in Fig. 4 in the main article’s body. Panels **a**, **b** and **c** show as a function of the applied flux Φ , respectively, the DC voltage, the flux-to-voltage transfer function (obtained by numerical differentiation) and the differential conductance (estimated by finite differences from the voltage traces recorded for $I_b = 4.3, 4.35, 4.4\text{ nA}$). The spectral characteristics of the amplified signal (green/blue traces: individual-channel power spectral density $\mathcal{A}_{1,2}$, black trace: cross-spectral density \mathcal{X}_{12} , gray shading: readout noise level estimate) are presented in panels **d-f** for three illustrative flux working points. Panel **d** corresponds to zero first-order response ($\Phi/\Phi_0 = 0.5$), while panels **e** and **f** are relative to the device being tuned for highest responsivity and best noise-equivalent flux resolution, respectively.

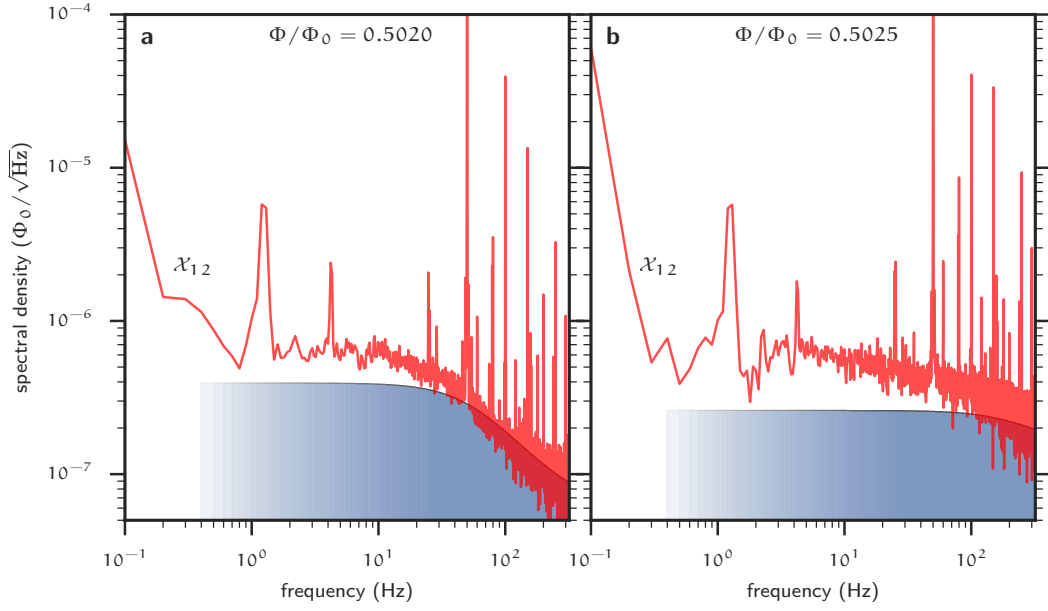


Figure 3. Cross-spectral density \mathcal{X}_{12} (red trace) and readout noise estimate (gray shading) in magnetic flux units. Panel **a** and **b** correspond, respectively, to the device tuned for highest responsivity ($\Phi/\Phi_0 = 0.502$) and for best noise-equivalent flux resolution ($\Phi/\Phi_0 = 0.5025$).